Atmos. Meas. Tech. Discuss., 4, 6779–6809, 2011
www.atmos-meas-tech-discuss.net/4/6779/2011/
doi:10.5194/amtd-4-6779-2011

Atmospheric Measurement Techniques Discussions

Retrieval of aerosol optical depth and vertical distribution using O_2 A- and B-band SCIAMACHY observations over Kanpur: a case study

S. Sanghavi[1], **J. V. Martonchik**[1], **J. Landgraf**[2], **and U. Platt**[3]

[1]Jet Propulsion Laboratory, California Institute of Technology, MS 169-237, 4800 Oak Grove Drive, Pasadena, CA 91109, USA
[2]Netherlands Institute of Space Research (SRON), Sorbonnelaan 2, 3584 CA Utrecht, The Netherlands
[3]Institute for Environmental Physics, Im Neuenheimer Feld 229, 69120 Heidelberg, Germany

Received: 20 July 2011 – Accepted: 15 September 2011 – Published: 8 November 2011

Correspondence to: S. Sanghavi (suniti.sanghavi@gmail.com)

Published by Copernicus Publications on behalf of the European Geosciences Union.

Abstract

The vertical profiles of aerosol often provide a clear picture of transport processes, and are an indicator of elevated secondary aerosol formation or primary aerosol sources close to the surface. The vertical extent of clouds and aerosols also governs the sign and magnitude of their net radiative forcing.

Ground- and satellite-based lidar measurements presently provide much of this information, however their sampling of 3-D data is limited due to infrequent, sparce or uneven coverage. From a remote-sensing perspective, retrievals of many trace-gases suffer from uncertainties due to aerosol and would benefit from co-located information on the amount and vertical distribution of aerosol loading. This motivates the development of complementary methods to retrieve vertical information on aerosols using satellite data, which have the advantage of more frequent global coverage. SCIAMACHY onboard ENVISAT provides spectral data at moderate resolution in the UV/VIS including the O_2 A- and B-bands, which contain vertical information due to the known vertical profile of O_2. We make combined use of these bands in an optimal estimation based algorithm applicable both over bright and dark surfaces to retrieve the parametrized vertical profile of aerosol, in addition to the optical thickness from SCIAMACHY data. We present a case study over Kanpur, India, showing good agreement with coincident AERONET data, capturing seasonal cycles and a periodic wind-blown dust event over Kanpur.

1 Introduction

The importance of knowledge of the vertical distribution of aerosol is punctuated by events such as the Ejyafjallajökull volcanic eruption of April 2010, which caused a long and far-reaching disruption of air traffic. Less cataclysmic, but still of interest, are the everyday effects of aerosol/cloud height in various areas ranging from public health

AMTD
4, 6779–6809, 2011

(Yang et al., 2008; Pope III, 2000; Liu et al., 1991), climate prediction (Menon et al., 2002; Lohmann and Feichter, 1997; Charlson et al., 1992, 1991; Mitchell Jr., 1971), advective transport studies (Colarco et al., 2004; Balkanski et al., 1993), etc. From the perspective of remote sensing of trace gases, aerosols frequently impose severe uncertainties (Aben et al., 2007; Houweling et al., 2005; Boersma et al., 2004) that may be remedied by simultaneous, co-located knowledge of their vertical profile.

As already suggested in previous work (Heidinger and Stephens, 2010; Kokhanovsky and Rozanov, 2004; Koppers et al., 1997), the O_2 absorption bands contain information on the vertical structure of atmospheric scattering by virtue of the known exponential profile of atmospheric oxygen. While the above-mentioned studies focus on determining the vertical extent of clouds using the O_2 A-band, we extend the measured data in our retrieval to include the weaker O_2 B-band as well. This provides, in addition to increased sensitivity to atmospheric layers close to the surface (which becomes especially important at the moderate spectral resolution typical of SCIAMACHY), also the benefit of a different, generally lower, surface albedo for retrievals over land, providing, as we show with the aid of sensitivity studies in Sect. 4, an additional constraint to our retrieval problem. This results in an ability to quantify not only effective cloud heights for cloudy scenes, but also to retrieve the parametrized form of the aerosol column for hazy scenarios. The simultaneous use of the two bands is often critical to removing redundancies due to the non-monotonic character of the signal with respect to aerosol loading (Sanghavi et al., 2010) as we have seen in retrievals from SCIAMACHY measurements described in Sect. 5.

We have applied our algorithm to SCIAMACHY data obtained over Kanpur, India, during the year 2003. Located in the Indo-gangetic plains, this is an area of considerable interest for studies of aerosol. It hosts an AERONET site that we use to validate our results. Predominantly due to the tropical location of Kanpur, the surface albedo does not display much seasonality due to the absence of large-scale changes in vegetation or snow cover, as a result of which the surface albedo can be assumed to be constant throughout the year. The subtropical, non-coastal location of Kanpur also

AMTD
4, 6779–6809, 2011

increases the probability of cloudless scenarios and, thus, the number of measurements that truly qualify as hazy without clouds.

Given the large size of the SCIAMACHY pixel, we do not attempt in this work to filter out clouds. Our motivation is to make maximum use of all measurements by attempting to find an effective representation of the scenario. Consequently, we retrieve more clouds than aerosols in the monsoon season (mid-June through September). As we show in the following, their retrieved heights and high optical thicknesses appear to be quite feasible inspite of the assumption of an urban aerosol as our underlying model. Using this kind of retrieval simply to indentify clouds while maintaining appropriate flags to indicate low confidence in the absolute value of the retrieved optical thickness, we see value in retaining this kind of "effective" approach which tolerates the presence of both cloud and aerosol in the observed scenario.

2 Retrieval algorithm

For our retrieval, we make a climatology-based (Stammes and Noordhoek, 2002) assumption of the aerosol microphysical parameters, which fixes the aerosol extinction coefficients, the single scattering albedos and the phase function for the central wavelengths of both the O_2 A- and B-bands to be used in the forward model. These values are assumed to be constant throughout the band-width. For the case-study over Kanpur, we assume the aerosol to be a relatively coarse urban absorbing type, having the microphysical parameters shown in Table 1. We determine the surface albedos for the two bands and their respective spectral gradients according to the method demonstrated in Sanghavi et al. (2010). We also assume a normalized lognormal vertical profile characterized by a peak height z_p and a peak width σ_p for the aerosol loading:

$$\rho_{aer}(z) = \frac{1}{\sqrt{2\,\pi}\,\sigma_p\,z}\,\exp\left[-\frac{(\log z - \log z_p)^2}{2\,\sigma_p^2}\right]. \quad (1)$$

AMTD
4, 6779–6809, 2011

Since aerosols close to the surface are likely to have exponentially decreasing number concentrations, and since an exponential profile can be closely approximated by making $z_p \to 0$, we consider the use of such a profile justified for aerosols occurring close to the ground. The other predominant scenario is the injection or production of aerosol at a finite height, e.g. by way of advection, a strong updraft, release from chimney stacks, or due to secondary aerosol formation, where a lognormal profile may be expected to form due to mixing in an atmosphere of exponentially falling density. We choose a priori values of $z_p = 1.2$ km and $\sigma_p = 0.85$ to approximate an exponentially falling profile with a scale height of 2 km, to conform with the generally expected profile of urban aerosols (Stammes and Noordhoek, 2002). We find that this has practically no bearing on the retrieved values. Furthermore, we choose a low a priori AOT of 0.05 to prevent overshooting to negative values of AOT during retrieval iterations.

Using these assumptions and inputs, we seek to retrieve the aerosol optical depth τ_{700} at 700 nm and the vertical profile parameters z_p and σ_p by using optimal estimation to invert the logarithm of reflectance measurements in the spectral ranges between 684–688 nm (O_2 B-band) and 757–774 nm (O_2 A-band). We discard wavelengths beyond 688 nm in the B-band, because of the presence at these wavelengths of interfering lines of water absorption. We choose the 700 nm wavelength for our AOT retrievals because it lies closely between the O_2 A- and B-bands as a result of which τ_{700} is less likely to propagate error due to any departure of the actual aerosol from the assumed aerosol type than, say, τ_{500} at the standard wavelength of 500 nm. For our assumed aerosol model, the optical thicknesses at the two wavelengths are related as follows:

$$\tau_{500} = 1.65 \cdot \tau_{700}, \quad (2)$$

which is large compared to the difference between τ_{700} and the optical thicknesses at the central wavelengths 686 nm and 765 nm, respectively:

$$\tau_{686} = 1.03 \cdot \tau_{700}$$

$$\tau_{765} = 0.87 \cdot \tau_{700}. \quad (3)$$

AMTD
4, 6779–6809, 2011

In order to gain flexibility from the assumed model, we allow $d\tau/d\lambda$ to vary by ±10 % about the value laid down by our choice of the aerosol model.

The relationship between the measurement data, denoted by the so called measurement vector $\boldsymbol{y}$ and the set of parameters to be retrieved, denoted by the state vector $\boldsymbol{x}$, is given by

$$\boldsymbol{y} = \mathbf{F}(\boldsymbol{x}) + \boldsymbol{\epsilon}, \tag{4}$$

where $\boldsymbol{\epsilon}$ is the retrieval error, which combines measurement error and the error due to the forward model $\mathbf{F}(\boldsymbol{x})$ used to approximate the physics of the measurement.

Optimal Estimation (Rodgers, 2000) provides the following variation of the Gauss-Newton iterative scheme for the inversion of our state vector:

$$\boldsymbol{x}_{i+1} = \boldsymbol{x}_\mathrm{a} + \left(\mathbf{K}_i^T \mathbf{S}_\epsilon^{-1} \mathbf{K}_i + \mathbf{S}_\mathrm{a}^{-1}\right)^{-1} \mathbf{K}_i^T \mathbf{S}_\epsilon^{-1} \left[\boldsymbol{y} - \mathbf{F}(\boldsymbol{x}_i) + \mathbf{K}_i(\boldsymbol{x}_i - \boldsymbol{x}_\mathrm{a})\right], \tag{5}$$

where $\boldsymbol{x}_i$ and $\boldsymbol{x}_{i+1}$ are consecutive iterations of the state vector to be retrieved, $\boldsymbol{x}_\mathrm{a}$ is the a priori state vector obtained from climatology, $\mathbf{S}_\mathrm{a}$ is the a priori covariance matrix, $\mathbf{S}_\epsilon$ is the measurement covariance matrix, and $\mathbf{K}_i$ is the Jacobian of the forward model $\mathbf{F}$ calculated at $\boldsymbol{x}_i$.

The forward model $\mathbf{F}(\boldsymbol{x})$ and the corresponding Jacobian $\mathbf{K}$ are computed using a linearized version of the Grant and Hunt Matrix Operator Method (GHMOM) radiative transfer model (Martonchik, 1975; Hunt and Grant, 1969).

The iterations are assumed to have converged when the difference in the solutions obtained during consecutive iterations is an order of magnitude smaller than the estimated error. Thus our test for convergence is

$$(\boldsymbol{x}_i - \boldsymbol{x}_{i+1})^T \mathbf{S}^{-1} (\boldsymbol{x}_i - \boldsymbol{x}_{i+1}) \lesssim n, \tag{6}$$

where n is the size of the state vector $\boldsymbol{x}$, and $\mathbf{S}$ is the a posteriori covariance matrix, given by

$$\mathbf{S} = \left(\mathbf{S}_\mathrm{a}^{-1} + \mathbf{K}_i^T \mathbf{S}_\epsilon^{-1} \mathbf{K}_i\right)^{-1}. \tag{7}$$

AMTD
4, 6779–6809, 2011

3 Jacobian matrix

The Jacobian matrix **K** is an $M \times N$ matrix, where M is the length of the measurement vector $\boldsymbol{y}$ and N is the length of the state vector $\boldsymbol{x}$, such that its elements consist of the derivative of the elements of forward model **F** (employed to simulate the measurement vector $\boldsymbol{y}$) with respect to the elements of $\boldsymbol{x}$, i.e.

$$K_{jk} = \frac{\partial F_j}{\partial x_k},\ j \in 1, \ldots, M,\ k \in 1, \ldots, N.$$

The Jacobian matrix is the main driver of the inverse solution and can provide rich insights into the physics of the retrieval problem. Hence, before applying the above concept to synthetic and real retrievals, we present an inspection of the Jacobian of an arbitrarily chosen aerosol scenario over three different surface conditions that will be revisited during the sensitivity study described in Sect. 4, viz. a black surface, for which the albedos around both A- and B-bands, ρ_A and ρ_B were taken to be zero, a high contrast continental surface, with $\rho_A \gg \rho_B$, typical of vegetation, and finally a moderate contrast dark continental surface, with $\rho_A \gtrsim \rho_B$, representative of dark, sparsely vegetated surfaces. For the high contrast surface, we assumed $\rho_A = 0.22$ and $\rho_B = 0.03$, for the moderate contrast dark surface, we took $\rho_A = 0.13$ and $\rho_B = 0.09$.

Figure 1 represents the black surface, where the top panels show the column of the Jacobian matrix corresponding to differentiation with respect to the aerosol optical thickness, τ_{700}. The middle and bottom panels represent derivatives with respect to the peak height z_p and the peak width σ_p, respectively. In each case, the left and right panels represent the B-band and the A-band, respectively. The spectra shown in black have been computed at a fine resolution of 0.002 nm. The red curves have been computed for the SCIAMACHY wavelength grid after convolution of the high resolution spectrum with the corresponding instrumental slit function (assumed to be gaussian with a FWHM of ≈0.4 nm).

In the following discussion, we define the "depth" of the radiance within the absorption lines relative to that in the continuum around it. Thus, an increase in the absorption

AMTD
4, 6779–6809, 2011

depth due to a change in a given aerosol parameter manifests itself in lower values of the Jacobian (a dip) at the absorption lines than in the continuum, while a decrease in the absorption depth is reflected in higher values of the Jacobian (a bump) at the absorption lines relative to the continuum.

In the top panels of Fig. 1, we notice that the depths of both the A- and B-bands increases with increasing optical thickness. This is a direct consequence of the longer geometrical path of light arriving at the detector after undergoing increased multiple scattering due to aerosol, which causes the absorbing wavelengths to suffer more extinction relative to the non-absorbing parts of the spectrum.

The middle and bottom panels, on the other hand, suggest a decrease in band depth with increasing z_p and σ_p. An increase in the peak height z_p causes more light to be scattered back without traversing the more absorbing lower layers of the atmosphere. Also to be noted is that the amount of multiple scattering is amplified by the number of ambient Rayleigh scatterers. Since the bulk of Rayleigh scatterers reside close to the surface, less multiple scattering occurs at higher altitudes, further shortening the net optical light path.

The decrease in band depth with respect to σ_p is much weaker than that due to z_p, to the extent that there is nearly no discernible change in the B-band. This is because an increase in σ_p merely results in a symmetrical redistribution of the aerosol towards the log normal tails. Strong absorption lines are more sensitive to higher atmospheric levels, since they are already saturated before they reach the lower layers. Weak lines, on the other hand, show less bias in their sensitivity since the atmosphere remains transparent at those wavelengths up to greater depths. This is reflected in the relatively large decrease in the depths of the strong absorption lines, resulting in a decrease in the A-band depth, while the depth of B-band remains nearly unchanged.

We now examine Fig. 2 representing the high contrast surface and notice that, contrary to the black surface, the depth of the A-band decreases with respect to optical thickness. In this case, higher optical thickness causes a "shielding effect" which prevents photons from traversing the lower atmosphere to reach the bright surface, thereby

AMTD
4, 6779–6809, 2011

decreasing the optical path length, leading to less absorption. The behavior with respect to z_p and σ_p, however, remains practically unchanged, since they do not have any impact on the net shielding effect of the aerosol.

Figure 3 represents the dark, moderate contrast surface in which the top left and right panels suggest that the depth of the B-band sees a slight increase and that of the A-band experiences as slight decrease with increasing optical thickness. In each of these cases, the surface is bright enough to be eclipsed by the shielding effect of aerosols resulting in a decrease in optical light path. However, the aerosols can also cause a sufficient increase in multiple scattering to eventually "outshine" the underlying surface and increase the optical light path. These opposing effects compete with each other in this case, with the former being slightly stronger in the A-band and the latter dominating slightly in the B-band. Again, the behavior with respect to z_p and σ_p remains nearly unchanged, suggesting that the dependence of the measurement on the vertical profile is not greatly affected by the surface albedo.

The patterns discussed above also evident in Fig. 4, which additionally allows for a direct comparison of Jacobian columns after convolution with the SCIAMACHY slit function for all surface types, the black, green and red curves representing the black, high contrast and dark moderate contrast surfaces, respectively, revealing the strong influence of the underlying surface albedo on the behavior of the reflectance with respect to changes in aerosol optical thickness.

4 Sensitivity studies

In order to test the robustness of the retrieval concept outlined in Sect. 2, we carried out sensitivity studies using synthetic SCIAMACHY data generated at different aerosol optical thicknesses and different lognormal vertical distributions, under the same three surface conditions presented in Sect. 3 , viz. a black surface, where both ρ_A and ρ_B were taken to be zero, a high contrast continental surface, with $\rho_A \gg \rho_B$, typical of vegetation, and a moderate contrast dark continental surface, with $\rho_A \gtrsim \rho_B$, representative

AMTD
4, 6779–6809, 2011

of dark, sparsely vegetated surfaces. Varying the aerosol optical thickness, $\tau_{aerosol}$, in each case between 0.05–2.0, the peak height, z_p, between 1–7 km, and the peak width, σ_p, between 0.5–1.0, under an assumed measurement error of 1 %, we compare the retrieved quantities to their true values.

In Fig. 5, the red asterisks show the retrieved aerosol optical thicknesses plotted against their true values, which are nearly coincident with the black 1:1 line between the x- and y-axes. The retrieval of vertical parameters is not exact at lower values of $\tau_{aerosol}$, as is apparent from the offset between the blue (for z_p) and magenta (for σ_p) circles from their respective "truth lines". This is to be expected, since at low aerosol optical thicknesses, the vertical distribution has a negligible contribution to the measurement, as a result of which the vertical profile parameters are more constrained by their a priori values than by the measurement. This situation is most apparent in the high contrast case, where increased multiple scattering due to the high surface albedo around the A-band causes more blurring of information on vertical profile. Almost paradoxically however, the retrieval over the black surface is not as good as that over the dark moderate contrast surface, showing that the difference in surface albedos in the A- and B-bands adds to the information content of the latter measurement. This is also true of the retrieval of the vertical profile parameters z_p and σ_p as shown in Figs. 6 and 7, respectively. In Fig. 6, the red asterisks represent the retrieved peak height z_p, plotted against the true value of z_p. The blue and magenta circles represent the retrieved values of $\tau_{aerosol}$ and σ_p, respectively, shown against their respective "truth lines". Again, the alignment of the asterisks along the black 1:1 line indicate the good retrievability of the peak height. This is less true of σ_p as shown by Fig. 7. Here, the red asterisks representing the retrieved values of σ_p are seen to depart considerably from some of the black 1:1 lines. We see an overestimation of low σ_p in the high contrast case, which is likely to be a result of blurring due to increased multiple scattering around the O_2 A-band, due to the high reflectivity of the surface. Also, in the case of the high contrast surface and the black surface, there occurs a loss of information at large σ_p, as a result of which the a priori constraints dominate the retrieval causing an

AMTD
4, 6779–6809, 2011

underestimation of the retrieved σ_p. The retrieved values also reflect an anti-correlation between the deviation from the truth of z_p and σ_p, as can be seen from the corresponding departure of the magenta circles representing z_p from its truth line. The blue circles representing $\tau_{aerosol}$, however, are still well-aligned with their truth line.

In summary, we can assume very robust retrievability for $\tau_{aerosol}$, good retrievability for z_p for log normal vertical distributions and a moderately good retrievability for σ_p, depending on the brightness and contrast of the underlying surface. The surface reflectances around the two bands and the differences thereof play an important role in determining how well posed the inversion problem is. Low surface reflectances reduce the amount of multiple scattering and hence allow more visibility through the vertical column, whereas the difference between the surface albedos adds to the number of constraints present in the inversion problem, thus adding to its information content. As a result, the combined use of the O_2 A- and B-bands allows good retrievals also over brighter surfaces, provided there is sufficient contrast between the albedos in the two bands.

We test this hypothesis over the city of Kanpur, located in a semi-arid region in the Indo-gangetic plains, over the year 2003, following the drought of 2002 (Kripalani et al., 2004).

5 Retrievals over Kanpur, India, using SCIAMACHY data

We have analyzed SCIAMACHY measurements obtained during 51 overpasses in 2003 over Kanpur. Based on the method of maximum relative contrast (Sanghavi et al., 2010), we assigned a clear sky scenario to 7 March 2003, corresponding to a surface albedo $\rho_A = 0.21$ and $\rho_B = 0.07$ around the A-and B-bands, respectively. Our method calculates the "apparent lambertian equivalent albedo (ALEA)", ρ, obtained by calculating the lambertian surface albedo that would produce the same reflectance at a given wavelength for an aerosol/cloud-free atmosphere as that measured by the satellite instrument. By calculating the value of ALEA at two different wavelengths, one near

AMTD
4, 6779–6809, 2011

the A-band, ρ_A, and the other near the B-band, ρ_B, we compute the "relative contrast" of a given scenario as $(\rho_A - \rho_B)/(\rho_A + \rho_B)$. For a given geometry, the relative contrast is found to decrease monotonically with increasing aerosol loading. Building a time series of the relative contrasts of all measurements available over a given location, we assign a clear sky scenario to the one with maximum relative contrast.

Choosing coarse absorbing aerosol microphysics typical of the region (Stammes and Noordhoek, 2002) for our forward model, we applied the above inversion to the measurements after correcting them radiometrically using the correction factors recommended in Van Diedenhoven et al. (2007) and Noël (2004).

We do not apply cloud-filtering to remove completely or partially cloudy scenarios before applying our retrieval to a measurement. Instead, we attempt to use individual retrieval characteristics like optical thickness and the convergence properties of our retrieval iterations to identify different cloudy situations. We consider this approach useful in obtaining effective values of particulate contamination encountered in trace gas measurements, without having to discard large quantities of data simply because they do not fall into the category of "pure aerosol" or "pure cloud".

The application of the inversion to SCIAMACHY data requires some limitations to be borne in mind. The limitations are partly instrumental, viz. uncertainties in radiometric calibration that may lead to biases in the retrieval and the large footprint (30 km × 60 km) of the instrument, frequently making a homogenous representation of the observed scene implausible. The resulting departure from truth, combined with that due to forward-model assumptions with regard to aerosol microphysical properties and surface type, can limit the representability of the scenario being observed, possibly affecting the accuracy of the inversion.

Radiometric calibration issues may be alleviated by co-retrieving the correction factors under tight constraints, so as not to undermine the retrieval of aerosol parameters. Better representation of the observed scenario may be achieved by employing better climatological data whenever available. However, little can be done to eliminate pixel inhomogeneities, especially those in the form of partially clouded scenes. This results

AMTD
4, 6779–6809, 2011

in fits that frequently lie outside of the limits set by measurement error, since the uncertainty in the retrieval predominantly stems from the lack of accurate representation by the forward model. This is a problem endemic to aerosol retrievals in general, which is exacerbated in the case of the SCIAMACHY instrument due to its large pixel size, and hence cannot be completely eliminated.

To deal with such limitations, we iterate our retrieval for a total of $N_{max} = 12$ times, computing the least squares mean of the resultant fit for each iteration, and choose the result of the iteration that produces the smallest least square mean value. In most cases of low AOT and very high AOT, the solution produces its best least squares fit at an iteration smaller than N_{max}, after which it remains fairly constant. This may be attributable to the better representability of such scenarios due to increased homogeneity. Other scenarios (usually corresponding to intermediate values of AOT) produce different solutions corresponding to comparable least squares fits, undermining the confidence with which we can choose a given solution. This includes problems involving oscillation between generally two possible solutions, a frequent cause of which is the degeneracy of measurements with respect to aerosol loading. As explained in Sanghavi et al. (2010), the degeneracy is caused by more than one aerosol scene corresponding to the same reflectance within a given channel. The simultaneous use of the A- and B-bands decreases the probability of occurrence of such oscillations.

Figure 8 shows a typical fit with a SCIAMACHY measurement. Since the quality of our retrievals vary with the scene being observed, we have flagged our retrievals "good", "oscillating" or "bad". A "good" convergence is said to occur when the model succeeds in arriving at a stable solution for which the modeled reflectance lies within the error bounds of the retrieval. The solution can be made unstable by the presence of an oscillation when two competing solutions are present. This is when we select the one with the lower least squares fit and flag the solution "oscillating". In cases where there is neither a stable nor oscillating solution, the retrieval is flagged as "bad".

The aerosol/cloud optical thicknesses retrieved from SCIAMACHY data are color-coded according to the "goodness" of the fit and plotted against the corresponding

AMTD
4, 6779–6809, 2011

relative contrast in the upper panel of Fig. 9, which suggests that the "goodness" of our fit decreases with increasing optical thickness. This is not a surprising result, as scene inhomogeneities are also expected to increase with increasing optical thickness, causing a steady departure of the forward model from reality. The increase in optical thickness also correlates well with the decrease in relative contrast, as hypothesized in Sanghavi et al. (2010). Also, the relative contrast at low to intermediate values of aerosol loading show highest sensitivity to changes in viewing geometry, viz. solar and line-of-sight zenith angles and (to a lesser extent) the corresponding azimuth angles, as a result of which the spread in relative contrast is largest there. The conjecture of negative relative contrast corresponding mainly to cloudy or very hazy scenarios is also verified from these results.

The bottom panel of Fig. 9 shows the temporal progression of the optical thickness as quantified on the left ordinate as well as the relative contrast depicted on the right ordinate, confirming a good anti-correlation.

The retrieved vertical profiles are shown in Fig. 10, where the upper panel shows a time-progression of the retrieved heights of maximum concentration along with the spread of the aerosol around that height, such that the gray region is bounded by lines corresponding to the heights at which the aerosol concentration falls to half the maximum value. The lower panel shows the form of the resulting vertical distributions. In the upper panel, peak heights corresponding to retrieved optical thicknesses greater than 5 are shown in cyan. It is found that all such cases also correspond to greater elevations, suggesting strongly that these retrievals may correspond to cloudy scenarios. The remaining retrievals may correspond to cloudless but also to partially cloudy scenarios. The residence of most aerosols over Kanpur between 0–5 km as suggested by these results can be confirmed by comparison with simultaneous twice-daily back-trajectory data (Pickering et al., 2001; Schoeberl and Newman, 1995) available from the AERONET website as well as later CALIPSO measurements (Winker et al., 2003).

Direct comparison of aerosol optical thickness with AERONET is not possible due to few simultaneous, co-located measurements. However, we have plotted AOT observed

AMTD
4, 6779–6809, 2011

by AERONET and SCIAMACHY observations having AOT ≤4 as a function of time in the top panel of Fig. 11, assuming other observations to have a greater degree of cloud-contamination. Although AERONET observations greatly outnumber SCIAMACHY retrievals, we can discern a general seasonality, causing the aerosol loading to increase from low values in the months of January–March steadily over the months of April–June, reaching a maximum at the beginning of the rainy monsoon season in mid-June. This is caused mainly due to the seasonal transport of wind-blown dust across the Indo-Gangetic plains (Bhattacharjee et al., 2007). During the monsoon period, which extends from mid-June through the end of September, cloudy scenes become frequent, reflected by decimated AERONET observations and resulting in a high degree of cloud contamination in SCIAMACHY retrievals. The months of October-December see a return of the aerosol loading to the initial "background" values, thus closing an annual cycle.

A comparison of monthly mean data, as shown in the middle and bottom panels of Fig. 11 helps quantify the main differences between SCIAMACHY and AERONET observations. SCIAMACHY largely underestimates low optical thicknesses, as seen in the periods January–March and October–December. This can be explained by the time-series method used to determine the surface albedo over Kanpur, which cannot correct for background aerosol that is always present over the given location. As a result, days of comparably low aerosol loading are regarded as almost haze-free by the inversion algorithm due to the "invisibility" of background aerosol in the inversion. Other months, on the other hand, see an overestimation due to cloud contamination that occurs in SCIAMACHY measurements due to the lack of a cloud filter.

AMTD
4, 6779–6809, 2011

6 Conclusions

In the work presented in this paper, we have made use of spectra obtained at medium resolution (≈1 nm) around the O_2 A- and B-bands of absorption to retrieve aerosol optical depth and the vertical profile of the aerosol using optimal estimation. Our method is applicable over both bright and dark surfaces, as long as the bright surface has sufficient contrast between the albedos near the two bands. Fortunately, this is true for most terrestrial surfaces (Baldridge et al., 2009). We have demonstrated using Jacobian matrices, sensitivity studies and retrieval examples that a combined use of the A- and B-band spectra helps remove redundancies while also improving the information content of the inversion problem. Sensitivity studies show a very robust retrievability of the AOT and good retrievability of the vertical profile. We have applied the retrieval to SCIAMACHY observations over Kanpur, India, through the year 2003. Notwithstanding uncertainties in instrumental radiometric calibration and the large footprint of the instrument, we could achieve good agreement with AERONET measurements of optical thickness and (retroactively) CALIPSO measurements of aerosol vertical distributions. We could obtain a very good anti-correlation between the retrieved optical thickness and the "relative contrast" introduced in Sanghavi et al. (2010). The conjecture of negative relative contrast corresponding mainly to thick clouds was verified.

The results obtained in this case-study may be translated on a larger scale to provide vertical information on aerosols with greater and more frequent coverage than instruments employing LIDAR. While LIDAR can provide a more differentiated view through the atmospheric column and is ideal for purposes of validation, our method has the advantage of providing a robust and inexpensive means of obtaining larger-scale vertical information on aerosols and clouds.

Acknowledgements. The bulk of this work was carried out as part of Suniti Sanghavi's PhD thesis. She would like to express her gratitude to Ulrich Platt for his support and ackowledge the IMPRS for awarding her with the scholarship that funded this work.

AMTD
4, 6779–6809, 2011

References

Aben, I., Hasekamp, O., and Hartmann, W.: Uncertainties in the space-based measurements of CO_2 columns due to scattering in the Earth's atmosphere, J. Quant. Spectrosc. Ra., 104, 450–459, 2007. 6781

Baldridge, A. M., Hook, S. J., Grove, C. I., and Rivera, G.: The ASTER spectral library version 2.0, Remote Sens. Environ., 113, 711–715, 2009. 6794

Balkanski, Y., Jacob, D., Gardner, G., Graustein, W., and Turekian, K.: Transport and Residence Times of Tropospheric Aerosols Inferred from a Global Three-Dimensional Simulation of 210Pb., J. Geophys. Res., 98, 20573, doi:10.1029/93JD02456, 1993. 6781

Bhattacharjee, P., Prasad, A., Kafatos, M., and Singh, R.: Influence of a dust storm on carbon monoxide and water vapor over the Indo-Gangetic Plains, J. Geophys. Res., 112, D18203, doi:10.1029/2007JD008469, 2007. 6793

Boersma, K. F., Eskes, H. J., and Brinksma, E. J.: Error analysis for tropospheric NO_2 retrieval from space, J. Geophys. Res., 109, D04311, doi:10.1029/2003JD003962, 2004. 6781

Charlson, R., Schwartz, S. E., Hales, J. M., Cess, R., Coakley Jr, J. A., Hansen, J. E., and Hofmann, D. J.: Climate forcing by anthropogenic aerosols, Science(Washington), 255, 423–423, 1992. 6781

Charlson, R. J., Langner, J., Rodhe, H., Leovy, C. B., and Warren, S. G.: Perturbation of the northern hemisphere radiative balance by backscattering from anthropogenic sulfate aerosols, Tellus A, 43, 152–163, 1991. 6781

Colarco, P. R., Schoeberl, M. R., Doddridge, B. G., Marufu, L. T., Torres, O., and Welton, E. J.: Transport of smoke from Canadian forest fires to the surface near Washington, DC: Injection height, entrainment, and optical properties, J. Geophys. Res., 109, D06203, doi:10.1029/2003JD004248, 2004. 6781

Heidinger, A. and Stephens, G.: Molecular line absorption in a scattering atmosphere, Part II: Application to remote sensing in the O_2 A band, J. Atmos. Sci., 57, 1615–1634, 2010. 6781

Houweling, S., Hartmann, W., Aben, I., Schrijver, H., Skidmore, J., Roelofs, G.-J., and Breon, F.-M.: Evidence of systematic errors in SCIAMACHY-observed CO_2 due to aerosols, Atmos. Chem. Phys., 5, 3003–3013, doi:10.5194/acp-5-3003-2005, 2005. 6781

Hunt, G. E. and Grant, I. P.: Discrete space theory of radiative transfer and its application to problems in planetary atmospheres, J. Atmos. Sci., 26, 963–972, 1969. 6784

AMTD
4, 6779–6809, 2011

Kokhanovsky, A. and Rozanov, V.: The physical parameterization of the top-of-atmosphere reflection function for a cloudy atmosphere-underlying surface system: the oxygen A-band case study, J. Quant. Spectrosc. Ra., 85, 35–55, 2004. 6781
Koppers, G. A. A., Jansson, J., and Murtagh, D. P.: Aerosal optical thickness retrieval from GOME satellite data in the Oxygen A band, in: Third ERS Symposium on Space at the service of our Environment, 414, p.693, 1997. 6781
Kripalani, R. H., Kulkarni, A., Sabade, S. S., Revadekar, J. V., Patwardhan, S. K., and Kulkarni, J. R.: Intra-seasonal oscillations during monsoon 2002 and 2003, Current Sci., 87, 325–331, 2004. 6789
Liu, S. C., McKeen, S. A., and Madronich, S.: Effect of anthropogenic aerosols on biologically active ultraviolet radiation, Geophys. Res. Lett., 18, 2265–2268, 1991. 6781
Lohmann, U. and Feichter, J.: Impact of sulfate aerosols on albedo and lifetime of clouds: A sensitivity study with the ECHAM4 GCM, J. Geophys. Res., 102, 13685, 1997. 6781
Martonchik, J.: Sulphuric acid cloud interpretation of the infrared spectrum of Venus, PhD Thesis, 1975. 6784
Menon, S., Hansen, J., Nazarenko, L., and Luo, Y.: Climate effects of black carbon aerosols in China and India, Science, 297, 2250, 2002. 6781
Mitchell Jr., J.: The effect of atmospheric aerosols on climate with special reference to temperature near the earth's surface, J. Appl. Meteorol., 10, 703–714, 1971. 6781
Noël, S.: Determination of correction factors for SCIAMACHY radiances and irradiances, Tech. Note IFE-SCIA-SN-20040514, University of Bremen, Bremen, Germany, 2004. 6790
Pickering, K. E., Thompson, A. M., Kim, H., DeCaria, A. J., Pfister, L., Kucsera, T. L., Witte, J. C., Avery, M. A., Blake, D. R., Crawford, J. H., Heikes, B. G., Sachse, G. W., Sandholm, S. T., and Talbot, R. W.: Trace gas transport and scavenging in PEM-Tropics B South Pacific Convergence Zone convection, J. Geophys. Res., 106, 32591, 2001. 6792
Pope III, C.: What Do Epidemiologic Findings Tell Us about Health Effects of Environmental Aerosols?, J. Aerosol Med., 13, 335–354, 2000. 6781
Rodgers, C.: Inverse methods for atmospheric sounding: Theory and practice, 2000. 6784
Sanghavi, S., Platt, U., and Landgraf, J.: Bichromatic method for identification of clear-sky scenarios over ground pixel viewed from space, Appl. Optics, 49, 3282–3290, 2010. 6781, 6782, 6789, 6791, 6792, 6794
Schoeberl, M. and Newman, P.: A multiple-level trajectory analysis of vortex filaments, J. Geophys. Res., 100, 25801, 1995. 6792

AMTD
4, 6779–6809, 2011

Stammes, P. and Noordhoek, R.: OMI algorithm theoretical basis document volume III: clouds, aerosols, and surface UV irradiance, Tech. Rep. ATBD-OMI-03, Version 2.0, 2002. 6782, 6783, 6790

Van Diedenhoven, B., Hasekamp, O. P., and Landgraf, J.: Retrieval of cloud parameters from satellite-based reflectance measurements in the ultraviolet and the oxygen A-band, Journal of Geophysical Research, 112, D15208, doi:10.1029/2006JD008155, 2007. 6790

Winker, D., Pelon, J., and McCormick, M.: The CALIPSO mission: Spaceborne lidar for observation of aerosols and clouds, in: Proceedings of SPIE, vol. 4893, p.1, 2003. 6792

Yang, E., Biazar, A., and Christopher, S.: CMAQ Air Quality Forecasts using Satellite Aerosol Retrievals, in: 10th Conference on Atmospheric Chemistry, 2008. 6781

AMTD

4, 6779–6809, 2011

Table 1. Aerosol microphysical parameters for a coarse, urban, absorbing aerosol (IA3). The bimodal size distribution is calculated as $p_{\mathrm{aer}}(r)\,\mathrm{d}r = \frac{1}{\sqrt{2\,\pi}\,r}\left\{\frac{1-\rho_{\mathrm{mode}}}{\log\sigma_{\mathrm{f}}}\exp\left[-\frac{(\log r-\log r_{\mathrm{f}})^2}{2\,(\log\sigma_{\mathrm{f}})^2}\right]\right.$ $\left.+\,\frac{\rho_{\mathrm{mode}}}{\log\sigma_{\mathrm{c}}}\exp\left[-\frac{(\log r-\log r_{\mathrm{c}})^2}{2\,(\log\sigma_{\mathrm{c}})^2}\right]\right\}\mathrm{d}r$.

Refractive index, real component, n_{r}	1.45
Refractive index, imaginary component, n_{i}	0.012
Effective radius, fine mode, r_{f}	0.109 µm
Effective width, fine mode, σ_{f}	1.56
Effective radius, coarse mode, r_{c}	0.804 µm
Effective width, coarse mode, σ_{c}	2.004
Mode fraction of coarse mode, ρ_{mode}	6.95e-4

AMTD
4, 6779–6809, 2011

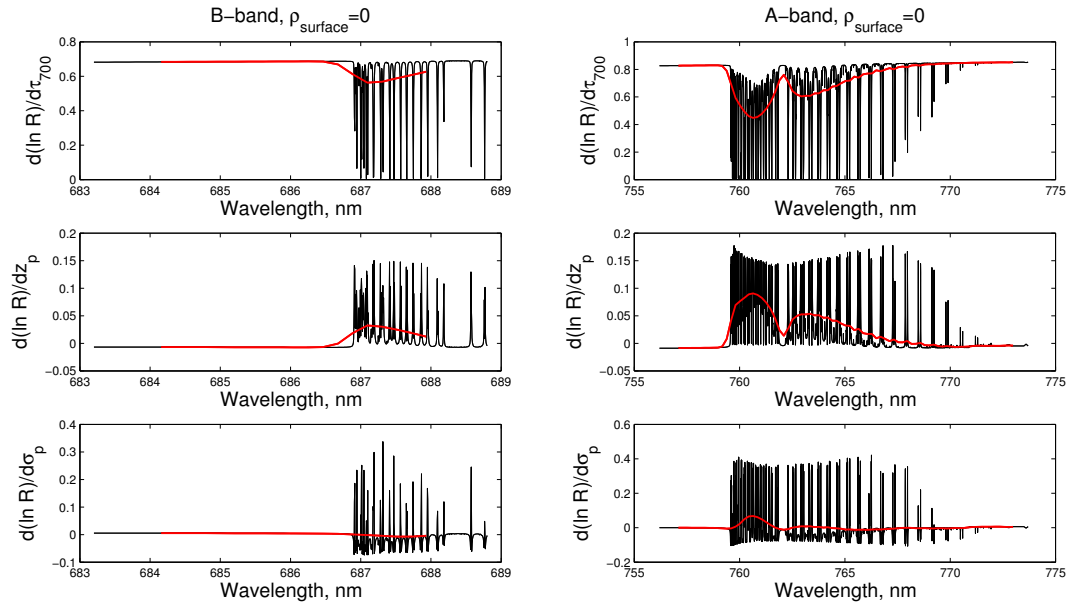

Fig. 1. A representation of the Jacobian matrix for a black surface. The spectra shown in black are computed at a fine resolution of 0.002 nm. The red curves are computed for the SCIAMACHY wavelength grid after convolution of the high resolution spectrum with a gaussian slit function having a FWHM of ≈0.4 nm. The top panels show the column of the Jacobian matrix corresponding to differentiation with respect to the aerosol optical thickness, τ_{700}. The middle and bottom panels represent derivatives with respect to the peak height z_p and the peak width σ_p, respectively. In each case, the left panel represents the B-band, while the right panel represents the A-band.

AMTD
4, 6779–6809, 2011

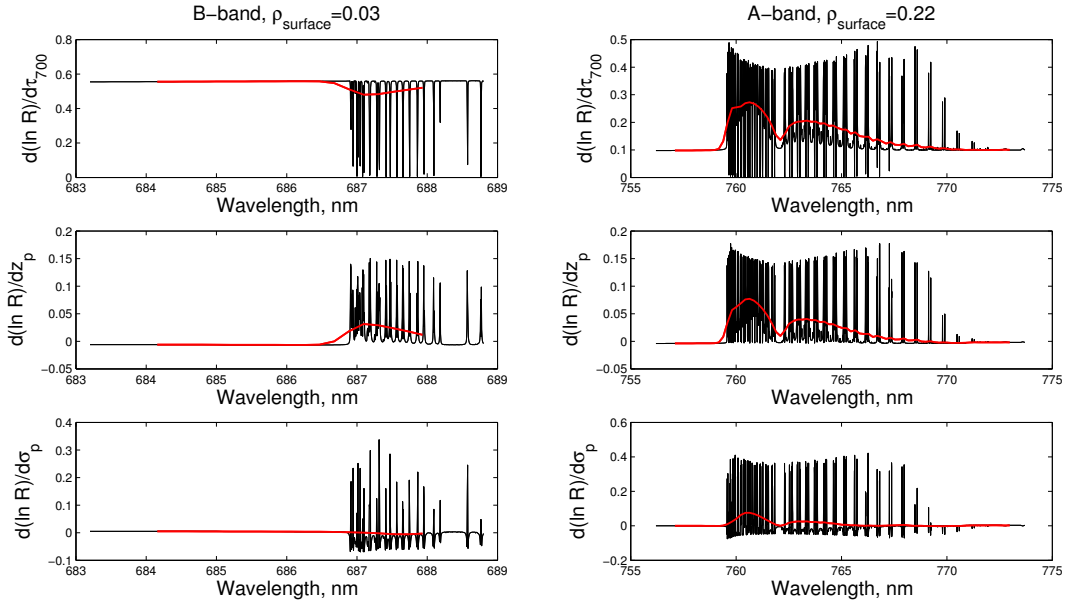

Fig. 2. Same as Fig. 1, but for a high contrast surface with $\rho_B = 0.03$ and $\rho_A = 0.22$. Note, however that the respective scales may differ.

AMTD
4, 6779–6809, 2011

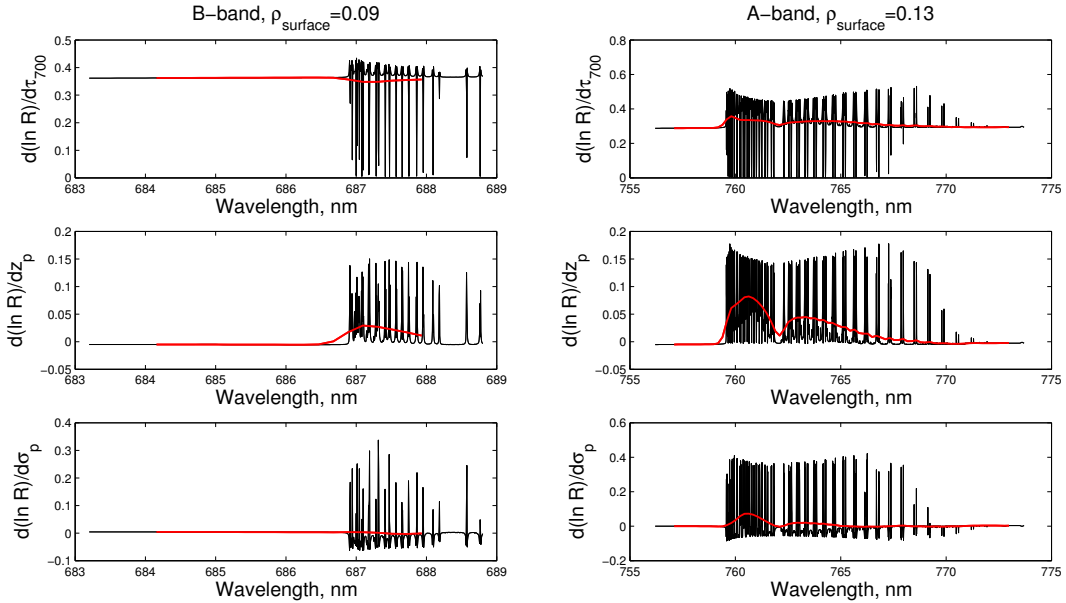

Fig. 3. Same as Fig. 1, but for a dark, moderate contrast surface with $\rho_B = 0.09$ and $\rho_A = 0.13$. Note, however that the respective scales may differ.

AMTD
4, 6779–6809, 2011

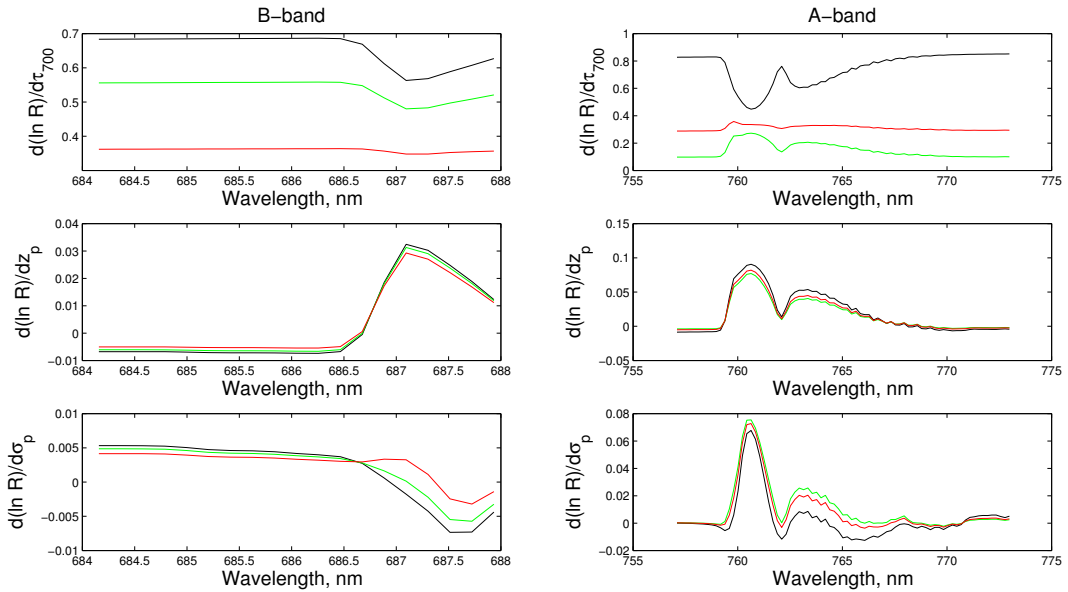

Fig. 4. Convolved Jacobian matrix representations for the black surface (black curve), high contrast surface (green curve), dark moderate contrast surface (red curve). The top, middle and bottom panels show derivatives with respect to optical thickness τ_{700}, peak height z_p and peak width σ_p, respectively.

AMTD
4, 6779–6809, 2011

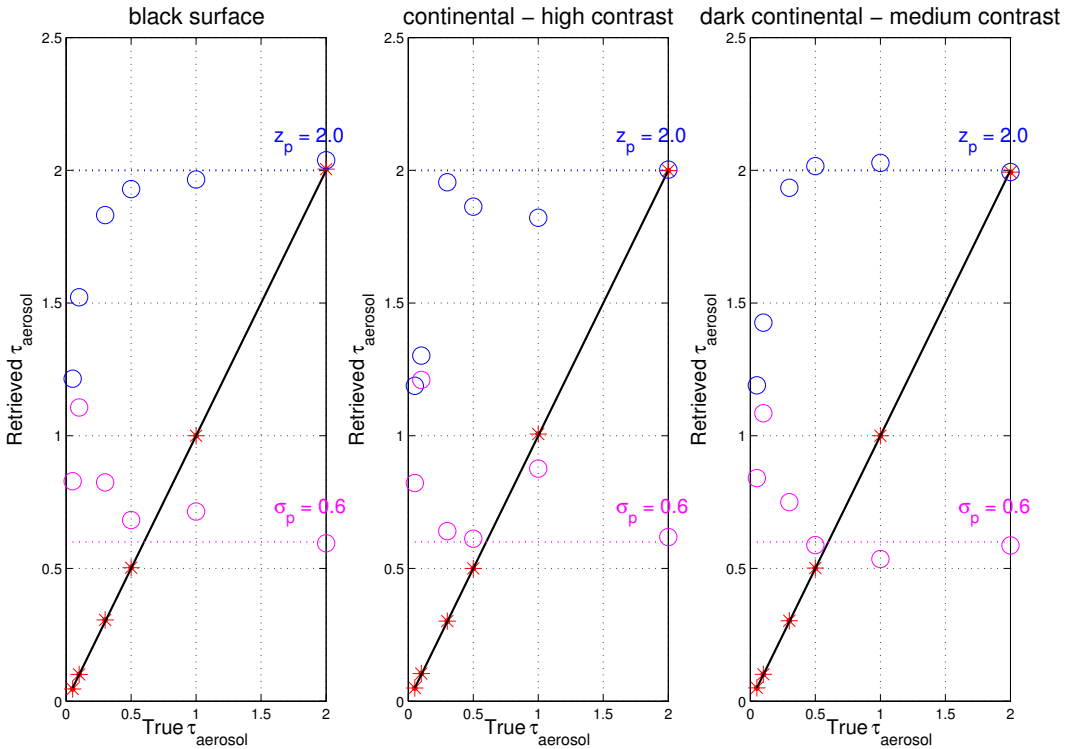

Fig. 5. Synthetic retrievals of aerosol optical thickness $\tau_{aerosol}$ (red asterisks), peak height z_p (blue circles) and peak width σ_p (magenta circles), for varying $\tau_{aerosol}$ and $z_p = 2$ km and $\sigma_p = 0.6$. Left panel: black surface, $\rho_A = \rho_B = 0$, middle panel: continental surface having high contrast, $\rho_A = 0.22$, $\rho_B = 0.03$, right panel: dark continental surface having moderate contrast, $\rho_A = 0.13$, $\rho_B = 0.09$.

AMTD
4, 6779–6809, 2011

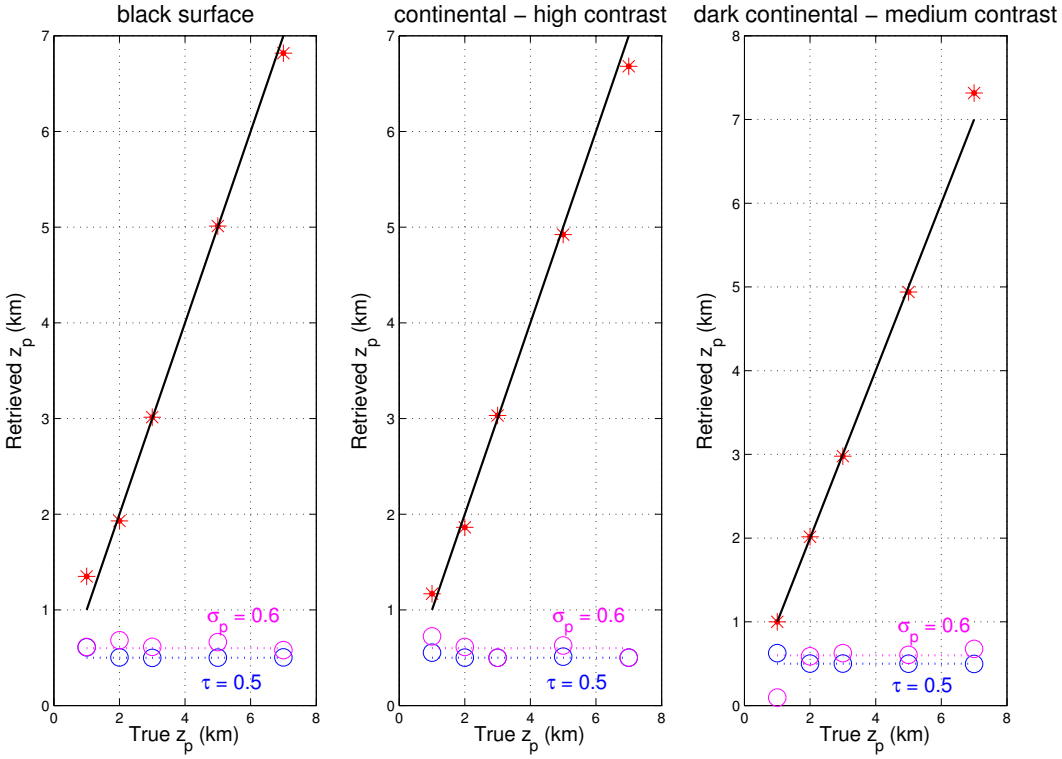

Fig. 6. Synthetic retrievals of the peak height of a lognormal aerosol vertical profile z_p (red asterisks), optical depth $\tau_{aerosol}$ (blue circles) and peak width σ_p (magenta circles), for varying z_p and $\tau_{aerosol} = 0.5$ and $\sigma_p = 0.6$. Left panel: black surface, $\rho_A = \rho_B = 0$, middle panel: continental surface having high contrast, $\rho_A = 0.22$, $\rho_B = 0.03$, right panel: dark continental surface having moderate contrast, $\rho_A = 0.13$, $\rho_B = 0.09$.

AMTD
4, 6779–6809, 2011

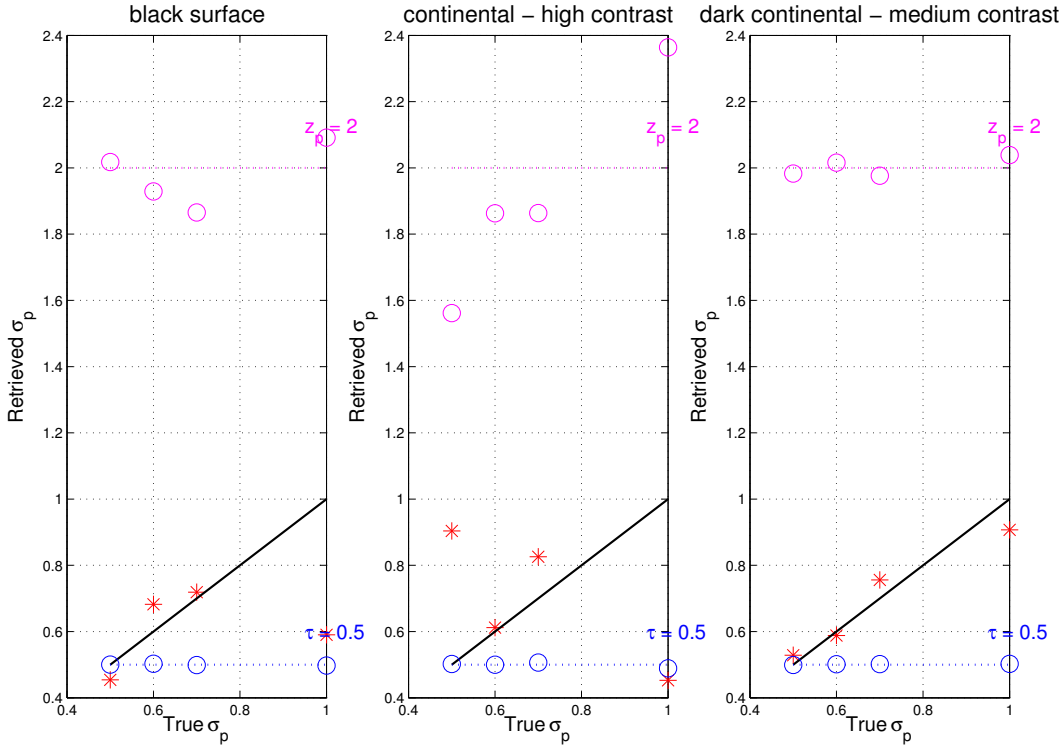

Fig. 7. Synthetic retrievals of the peak width of a lognormal aerosol vertical profile σ_p (red asterisks), optical thickness $\tau_{aerosol}$ (blue circles) and peak height z_p (magenta circles), for varying σ_p and $\tau_{aerosol} = 0.5$ and $z_p = 2$ km. Left panel: black surface, $\rho_A = \rho_B = 0$, middle panel: continental surface having high contrast, $\rho_A = 0.22$, $\rho_B = 0.03$, right panel: dark continental surface having moderate contrast, $\rho_A = 0.13$, $\rho_B = 0.09$.

AMTD
4, 6779–6809, 2011

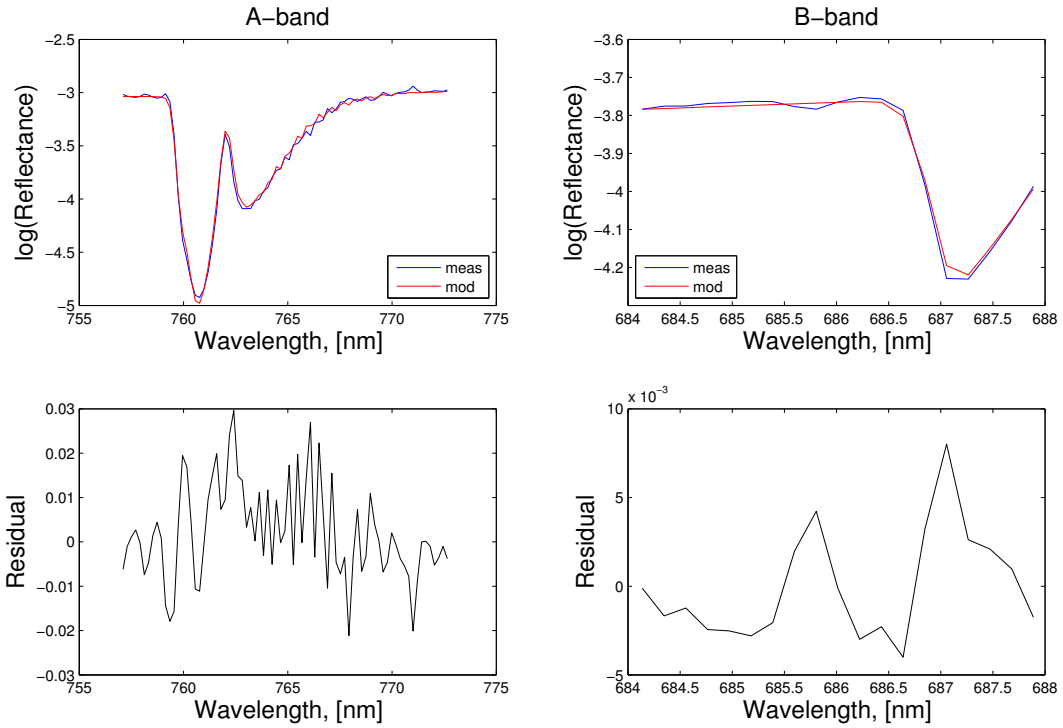

Fig. 8. A fit showing the O_2 A- and B-band spectra simulated by the forward model (red) against the spectra measured by SCIAMACHY (blue), in the upper left and right panels respectively. The log (Reflectance) indicates the natural logarithm of the measured and modeled reflectances. The bottom panels show the corresponding dimensionless residuals $\left(\frac{\log R_{\text{mod}} - \log R_{\text{meas}}}{\log R_{\text{meas}}}\right)$ given here by the difference of the two spectra relative to the measurement.

AMTD
4, 6779–6809, 2011

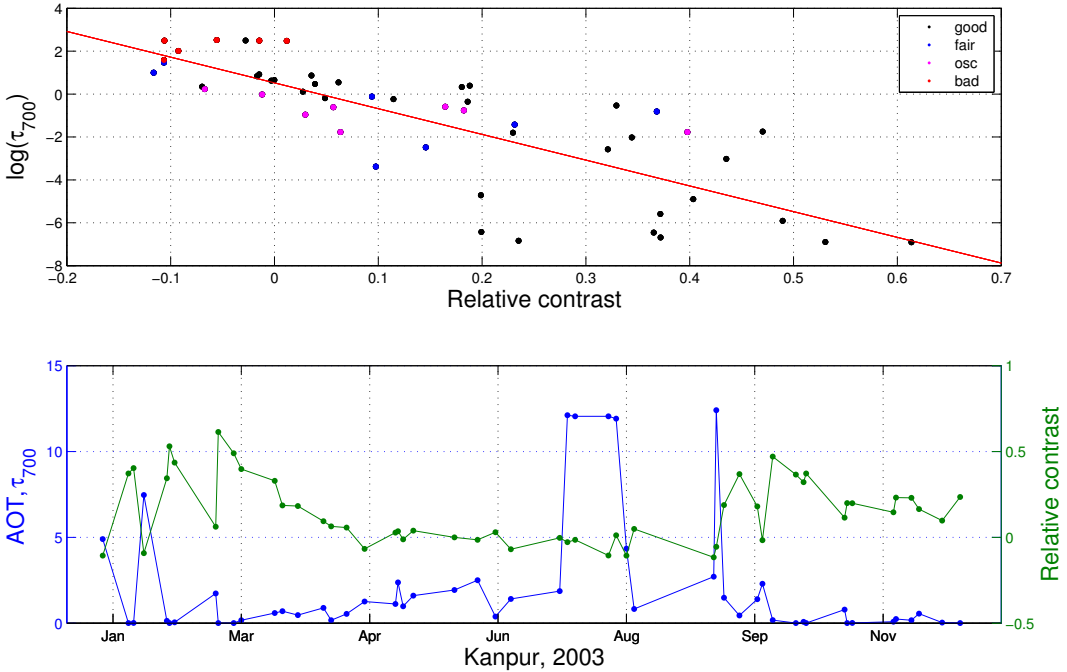

Fig. 9. Upper panel: the natural logarithm of the retrieved AOT plotted against the corresponding relative contrast. The points are color-coded according to the goodness of the retrieval, with black denoting a good fit, blue denoting fair, magenta representing the presence of oscillation, and red denoting a bad convergence. The red line represents a linear fit of the points with respect to relative contrast. Lower panel: a time series of the retrieved AOT plotted along the left y-axis, and the relative contrast plotted on the right y-axis.

AMTD
4, 6779–6809, 2011

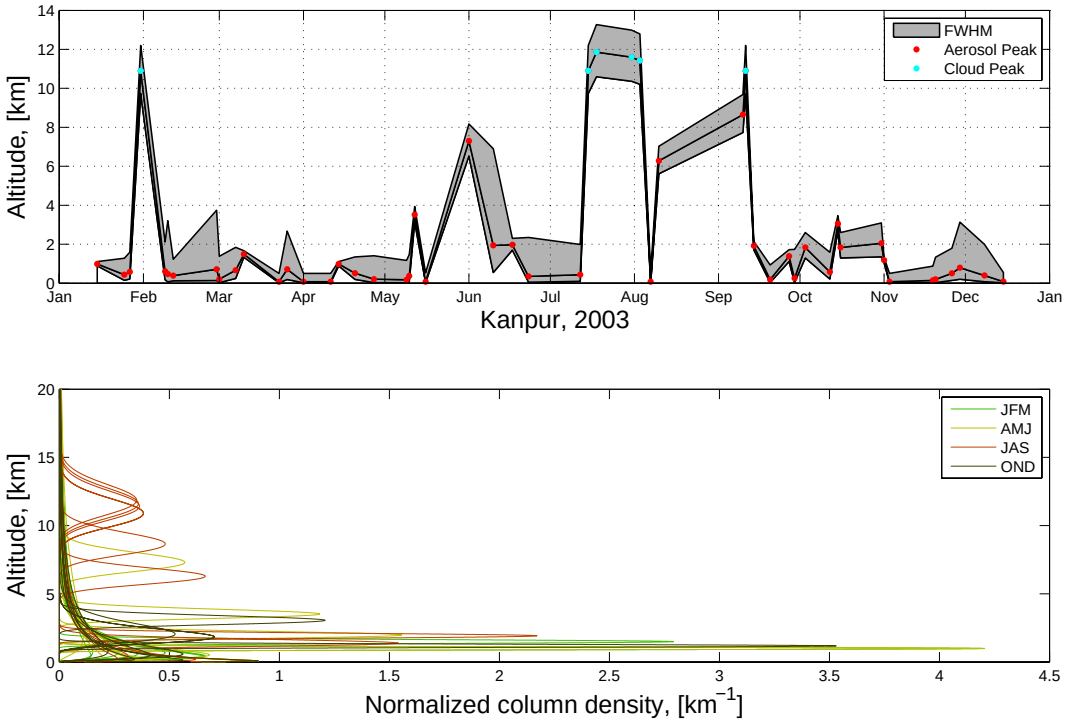

Fig. 10. Upper panel: a time series of retrieved heights of maximum aerosol concentration, represented by red dots for $\tau_{700} <= 5.0$, and cyan dots for $\tau_{700} > 5.0$. The black lines bounding the gray region around the dots represent heights at which the aerosol concentration is half its maximum value. Lower panel: a representation of each lognormal vertical profile retrieved in the case-study over Kanpur. The x-axis may be regarded as the probability density function for the aerosol to be present at a given altitude, hence the unit [km^{-1}]. The retrievals are color-coded by season as shown in the legend. The wet months of July, August and September stand out due to their high altitude profiles, mostly attributable to clouds.

AMTD
4, 6779–6809, 2011

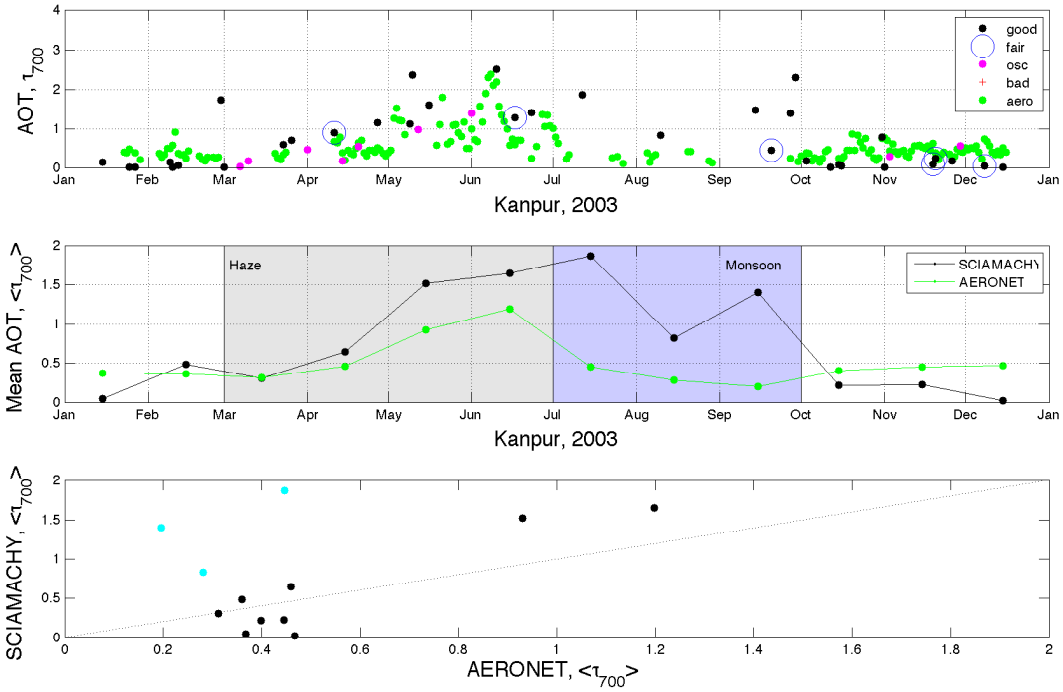

Fig. 11. Top panel: a time series of all AERONET measurements of AOT (675 nm) at Kanpur over the year 2003 (green dots), all SCIAMACHY retrievals of $\tau_{700} <= 4$, color coded according to the goodness of the retrieval. Middle panel: a time progression of the monthly means of both sets of data, AOT measured by AERONET (green) and those retrieved from SCIAMACHY (black dots). Lower panel: a scatter plot of SCIAMACHY monthly means of AOT against AERONET values. Strongly cloud contaminated (SCIAMACHY) data are color-coded cyan.

AMTD
4, 6779–6809, 2011